Nanoscale

RSC Publishing

PAPER

View Article Online
View Journal | View Issue

Cite this: *Nanoscale*, 2013, **5**, 11928

Orthorhombic KSc_2F_7:Yb/Er nanorods: controlled synthesis and strong red upconversion emission†

Yujie Ding,[a] Xue Teng,[c] Hao Zhu,[a] Lili Wang,[c] Wenbo Pei,[bc] Jun-Jie Zhu,*[a] Ling Huang*[bc] and Wei Huang*[b]

Received 12th April 2013
Accepted 21st June 2013

DOI: 10.1039/c3nr01840g

www.rsc.org/nanoscale

For the first time, we have synthesized orthorhombic phase KSc_2F_7:20%Yb/2%Er (KSc_2F_7:Yb/Er) nanorods and further studied the crystal structure and morphology evolution, as well as their upconversion (UC) properties under varying F^- contents and reaction temperatures. Different from β-$NaYF_4$:20%Yb/2%Er ($NaYF_4$:Yb/Er) nanorods that usually give strong green UC luminescence, strong red UC emission was observed in KSc_2F_7:Yb/Er nanorods under 980 nm laser excitation. Their UC mechanisms are further analyzed and compared. This study provides a novel type of rare earth nanorods with strong red UC emissions which have great potential in high resolution 3-dimensional bioimaging, color displays, solid-state lasers, and photocatalysis.

1 Introduction

The partially filled 4f orbitals of rare earth elements are buried beneath the 6s, 5p, and 5d orbitals, which weakens the coupling between the 4f orbitals and the surrounding ligands. This enables the transitions of the 4f electrons between the f–f and f–d orbitals and imparts rare earth ions with very rich spectroscopic properties, which possess unique potential in color device displays, lighting, medical and biological labels, solar cells, and solid-state lasers.[1–7] Compared to conventional luminescent materials like organic fluorescent dyes and quantum dots (QDs), lanthanide-doped materials exhibit distinct optical properties, such as sharp emission bandwidths, long luminescence lifetimes and high photostability. For instance, they display neither photoblinking on the millisecond and second time scales nor photobleaching even with hours of continuous excitation.[8–11] In particular, lanthanide-doped nanomaterials comprising proper host–dopant combinations can convert near infrared (NIR) long-wavelength excitation radiation into short-wavelength visible emissions, which makes them promising biological probes with deep tissue penetration and low autofluorescence background.[12,13] These unique anti-Stokes emitters, now widely known as UC nanomaterials, have attracted considerable interest because of their wide applications in the areas of high resolution 3-dimensional bioimaging, photodynamic therapy, photocatalysis,[14–17] and so on.

Of the various UC nanomaterials, fluoride nanocrystals such as $NaYF_4$,[18–20] $NaGdF_4$,[21–23] $LiYF_4$,[24,25] $KMnF_3$,[26] CaF_2,[27] and $BaYF_5$[28,29] have aroused predominant interest due to their low phonon energies and decent optical transparency over a wide range of wavelengths. Among them, the β phase $NaYF_4$ nanomaterial is thought by far one of the most efficient UC host crystals, however it is only good at limited UC emission wavelengths and the search for novel luminescent nanomaterials with desired UC emission windows to satisfy various applications still remains an urgent and challenging topic.

In the periodic table, Scandium (Sc) sits at not only the very top of group IIIB, but also the very beginning of the transition metals, and its distinct atomic electronic configuration may produce optical properties different from those of Y/Ln-based nanomaterials. Indeed, our group has proved that not only is the crystal structure of the Sc-based nanomaterials easily affected by the synthetic environment, but the UC emission is also different from those of Y/Ln-based nanomaterials.[30] Unfortunately, except this report, there are very few reports on the synthesis and optical properties of Sc-based nanomaterials with different chemical compositions and/or morphologies.

What is more, the majority of the previous studies on Y/Ln-based nanomaterials are focused on nanoparticles, while nanorods are seldom reported.[31–33] One reason might be that the crystal structures of Y/Ln-based nanomaterials are not as sensitive as that of Sc, to the synthetic environment, the other reason is that to get nanorods, stringent synthetic conditions or high levels of dopant of another type of rare earth element are often needed.[32] However for the case of Sc, we found that the nanorods can be easily synthesized by simply adjusting the amount of F^- or the reaction temperature.

[a]*State Key Laboratory of Analytical Chemistry for Life Science, School of Chemistry and Chemical Engineering, Nanjing University, Nanjing, 210093, China. E-mail: jjzhu@nju.edu.cn*

[b]*Institute of Advanced Materials, Nanjing Tech University, Nanjing, 210009, China. E-mail: iamlhuang@njut.edu.cn; iamwhuang@njut.edu.cn*

[c]*School of Chemical and Biomedical Engineering, Nanyang Technological University, 637457, Singapore. E-mail: lhuang@ntu.edu.sg*

† Electronic supplementary information (ESI) available: See DOI: 10.1039/c3nr01840g

2 Experimental

2.1 Chemicals

$ScCl_3 \cdot 6H_2O$ (99.99%), $YbCl_3 \cdot 6H_2O$ (99.99%), $ErCl_3 \cdot 6H_2O$ (99.9%), KOH (98%), NH_4F (98%), 1-octadecene (90%) and oleic acid (90%) were purchased from Sigma-Aldrich and used without further purification.

2.2 Material synthesis

The synthesis of KSc_2F_7:20%Yb/2%Er nanorods was developed *via* a modified literature procedure.[32] In a typical experiment, 1 mmol $RECl_3 \cdot 6H_2O$ (0.78 mmol $ScCl_3 \cdot 6H_2O$, 0.2 mmol $YbCl_3 \cdot 6H_2O$, 0.02 mmol $ErCl_3 \cdot 6H_2O$) was added to a 50 mL flask containing 15 mL oleic acid and 17.5 mL 1-octadecene and the solution was heated to 160 °C for 30 min and then cooled down to room temperature. Thereafter, 4 mL methanol solution of NH_4F (1.6 mmol) and KOH (1.0 mmol) was added into the solution and stirred for 30 min. After methanol evaporation, the solution was heated to 300 °C under argon environment for 1 h and cooled down to room temperature. The resulting nanorods were precipitated by the addition of ethanol, collected by centrifugation, washed with water and ethanol several times, and finally re-dispersed in cyclohexane.

2.3 Characterizations

The morphology and crystal structure of the nanorods were characterized by transmission electron microscopy (TEM) and high resolution TEM (HRTEM) using a JEOL-2100 TEM equipped with an Oxford Instruments energy-dispersive X-ray (EDX) system operating at 200 kV. The X-ray diffraction (XRD) measurements were performed on a Japan Shimadzu XRD-6000 diffractometer with Cu-Ka radiation ($\lambda = 0.15418$ nm); a scanning rate of 0.05 deg s^{-1} was applied to record the patterns in the 2θ range of 10–80°. UC luminescence spectra were recorded on a ZolixScan ZLX-UPL spectrometer where an external continuous-wave laser (980 nm) was used as the excitation source.

3 Results and discussion

Our experimental results have shown that the morphology and fluorescence intensity of the KSc_2F_7:Yb/Er nanorods can be easily manipulated by changing either the content of F^- or the reaction temperature, and more importantly it gives strong red UC emission, which is rarely seen in the rare earth doped UC nanoparticle studies.

Fig. 1 shows the effect of F^- content on the morphology, crystal structure, as well as the UC emission on $KScF_x$:Yb/Er nanomaterials. At high F^- content (4.0 mmol), the majority of the products were small nanoparticles and only a little nanorods was observed (Fig. 1a1). After the F^- content decreased from 4.0 to 1.6 mmol, all the nanoparticles turned into nanorods with an average aspect ratio of 12.5 : 1 (Fig. 1c1), while at the medium level of F^- content (2.8 mmol), the products are composed of a large amount of nanorods and small amount of nanoparticles (Fig. 1b1). This indicates that the F^- content has considerable influence on the shape evolution and low F^- content is beneficial for the formation of nanorods.

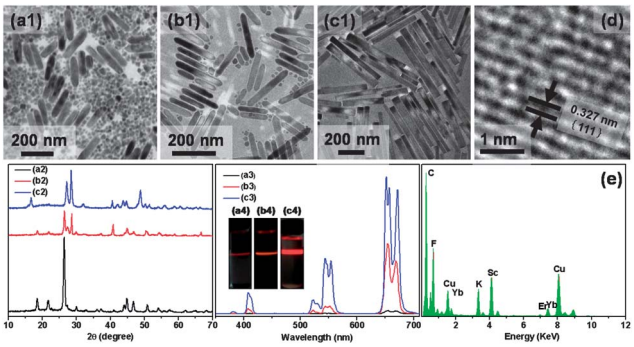

Fig. 1 TEM images of $KScF_x$ nanomaterials synthesized at (a1) 4.0, (b1) 2.8, and (c1) 1.6 mmol of F^- content respectively, their according XRD (a2, b2, c2), UC luminescence spectra (a3, b3, c3), and the according digital pictures (a4, b4, c4) of the samples in cyclohexane solution excited by 980 nm laser, respectively. (d) HRTEM image of the KSc_2F_7:Yb/Er nanorods in (c1) and (e) the EDX of the nanorods in (d).

Furthermore, from the XRD results we can see that the crystal structure of the nanomaterials changed from the predominantly end-centered monoclinic phase $KScF_4$:Yb/Er nanoparticles (JCPDS card 48-0677) at high F^- content (Fig. 1a2 and S1a2†) to pure orthorhombic phase KSc_2F_7:Yb/Er (JCPDS card 77-1321) nanorods at low F^- content (Fig. 1c2 and S1c2†), while both phases showed up at intermediate F^- content (Fig. 1b2 and S1b2†). The well-defined diffraction peaks in Fig. S1c2† indicate that the nanorods are at high crystallinity and all the peak positions match well those of the end-centered orthorhombic structure of the KSc_2F_7 nanorods with the nanocrystal cell parameters of $a = 1.064$ nm, $b = 0.654$ nm, and $c = 0.403$ nm. It is worth pointing out that the diffraction peaks have significant changes in the relative intensity compared to those of standard data, suggesting the existence of a preferential orientation for the nanorods.[30] The diffraction peaks also apparently shifted towards small values for two theta because of the larger ionic radii of Yb^{3+} ($r = 0.868$ Å) and Er^{3+} ($r = 0.89$ Å) compared to that of Sc^{3+} ($r = 0.745$ Å), indicating the formation of Yb/Er-doped KSc_2F_7 nanorods.[34–36]

The morphology development as a function of F^- content can be explained by the crystallization speed-controlled model.[37] The nanocrystal growth was initiated with the nucleation process between the F^- and rare earth oleate complex. The change of the monomer concentration in the solution is mainly caused by the nucleation process and the following growth process has relatively slight influence. Low concentration of F^- can significantly decelerate the particle crystallization rate and produce a relatively small amount of nuclei, leading to a relatively high monomer concentration in the solution. The growth of elongated nanocrystals should be initiated by high monomer concentration.[38] So, highly uniform nanorods were synthesized under the condition of low F^- content. On the contrary, high F^- content can enhance the crystallization speed, which results in the rapid depletion of the $RE(oleate)_3$ in the solution, and then the monomer concentration was reduced to a critical level rapidly. Since facets of the nanocrystals have different surface

energies, the corners and tips were rapidly smoothed by the excessive F^-.[37,39] As a result, smaller particles were obtained.

The UC emission intensity of the according products also changed with the varying amount of F^-. From the above discussion, we know that low F^- content favors the formation of nanorods and strong UC luminescence, with the pure nanorods (1.6 mmol of F^-) at the highest UC luminescence intensity (Fig. 1c3 and c4). We think this is because the orthorhombic (KSc_2F_7:Yb/Er) crystal structure has the proper atomic distance that assures the highest UC efficiency. While the cell parameters of monoclinic phase $KScF_4$:Yb/Er are, $a = 1.570$ nm, $b = 0.404$ nm, and $c = 1.327$ nm, which are much larger than those of orthorhombic phase KSc_2F_7:Yb/Er and don't favor the photon/electron energy combination, *i.e.*, low efficiency to work as a crystal host for UC purposes, and only very weak UC emission can be generated (Fig. 1a3 and a4). As a mixture of samples in Fig. 1a1 and c1, it is rational that the UC intensity of the product shown in Fig. 1b1 is at the medium level (Fig. 1b3 and b4).

The HRTEM image of a single nanorod in Fig. 1d provides clear details of the lattice arrangement of the atoms in the nanocrystalline host, indicating the highly crystalline nature of the material. The distance between the fringes (*d*-spacing) was measured to be 0.327 nm, corresponding to the distance of the {111} planes of the orthorhombic phase KSc_2F_7. Compositional analysis of an individual nanorod by EDX reveals that the nanorods are mainly composed of K, Sc, Yb, F and a small amount of Er element. The strong signals of Cu and C come from the TEM copper grid and the covered carbon film (Fig. 1e).

We further studied the effect of the reaction temperature on the morphology, crystal structure, and UC emission of the KSc_2F_7:Yb/Er nanorods. At 270 °C, only very short nanorods with the lengths of ~30 nm and the diameters of ~10 nm (followed with very little quantity of long ones) were obtained (Fig. 2a1). The long nanorods with increased amount are obtained at 280 °C, but still with irregular lengths and diameters (Fig. 2b1). When the temperature reached 300 °C, the product changed to pure and uniform nanorods with an average length at ~376 nm and diameter at ~30 nm (Fig. 2c1). It is obvious that only the 10–20 °C temperature variation has caused such a big difference of the nanorods as shown in Fig. 2a1–c1.

The formation of long nanorods from a colloidal suspension of spherical nanoparticles or short nanorods can be explained by the Smoluchowski aggregation kinetics.[40,41] The crystal growth mainly occurs *via* a multistep crystallographic specifically oriented attachment and the higher the coarsening temperature, the earlier the first stage ends.[42] Due to the high thermodynamic tendency for large surface area, small nanoparticles (nanorods) are highly metastable at high temperature compared to the equivalent bulk material. In our synthetic environment, even though oleic acid was used as a capping ligand, the nanorods don't seem to be at the equilibrium state and the ligand capping effect cannot completely inhibit the thermodynamic tendency for growth. Sequentially, small nanorods started to aggregate with each other at certain crystal facets to form large ones, and then the oleic acid molecules binding on the specific crystal surface of the nanorods were knocked off because of the high free energy driving force, high thermal energy, and the high energy of this specific crystal facet. The aggregated small rods then grew into long single rod.[43]

The crystal structure evolution is also monitored by the changes of the XRD signals shown in Fig. 2a2–c2. At 270 °C, only a very weak crystal signal can be seen, suggesting the poor crystallinity of the product at this low temperature. More and more crystal signals appeared when the temperature is increased to 280 °C and further to 300 °C, implying that the reaction temperature played a key role in the formation of the orthorhombic KSc_2F_7:Yb/Er nanorods.

The UC luminescence intensity kept increasing with the temperature, which is reasonable because higher temperature will result in large nanorods with relatively lower density of the surface defects compared to that of the small nanorods (with poor crystal structure) synthesized at low temperature, therefore large nanorods generate higher intensity of UC luminescence (Fig. 2c3) than those of small nanorods (Fig. 2a3). While the mixture of the small and large nanorods (Fig. 2b1) synthesized at intermediate temperature accordingly generates the UC luminescence at medium level intensity (Fig. 2b3). Similarly as discussed in Fig. 1, such dramatic UC luminescence intensity evolution is also clearly reflected in the digital pictures of their according colloidal solutions in cyclohexane (Fig. 2a4–c4).

Fig. 3a shows the room-temperature UC luminescence spectrum of KSc_2F_7:Yb/Er nanorods (Fig. S2a† shows the according TEM image) under 980 nm laser excitation where four major emission peaks at ~408, ~522, ~541 and ~650 nm, assigned to the $^2H_{9/2} \rightarrow {}^4I_{15/2}$, $^2H_{11/2} \rightarrow {}^4I_{15/2}$, $^4S_{3/2} \rightarrow {}^4I_{15/2}$ and $^4F_{9/2} \rightarrow {}^4I_{15/2}$ transitions, respectively, of erbium are observed. The dominant emission is located in the red luminescence range (650 nm), which is reflected in the digital picture of the KSc_2F_7:Yb/Er nanorods solution in cyclohexane (Fig. 3b). This

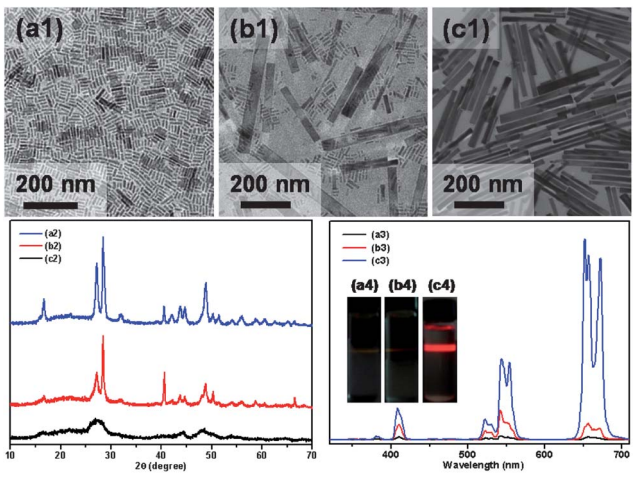

Fig. 2 KSc_2F_7:Yb/Er nanorods synthesized at (a1) 270 °C, (b1) 280 °C, and (c1) 300 °C. XRD (a2, b2, c2) and the UC luminescence (a3, b3, c3) spectra of the nanomaterials synthesized at the above temperatures respectively. The insert shows the digital pictures (a4, b4, c4) of the according samples in cyclohexane solution under 980 nm laser excitation.

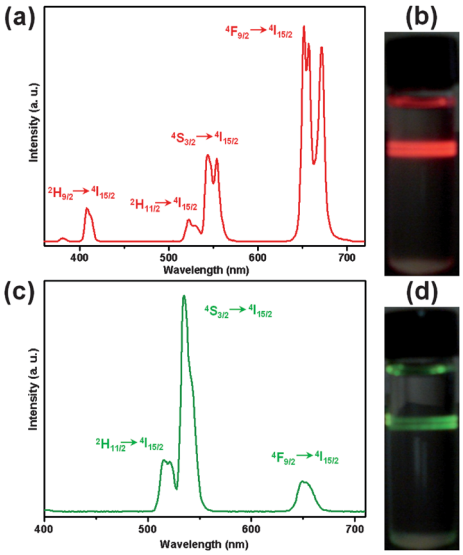

Fig. 3 UC luminescence spectra of (a) KSc_2F_7:Yb/Er and (c) $NaYF_4$:Yb/Er nanorods. (b) and (d) are the digital pictures of the according samples in cyclohexane solution under NIR laser excitation.

red emission is consistent with previous report but different from those of Y-based nanocrystal hosts, *i.e.*, β-$NaYF_4$:Yb/Er nanorods (Fig. 3d).[30,44]

For comparison, β-$NaYF_4$:Yb/Er nanorods were synthesized (Fig. S2b† shows the according TEM image)[44] and the UC emission spectrum is shown in Fig. 3c. We can see that the intensity of the red and green UC emissions from KSc_2F_7:Yb/Er nanorods is 4.8 and 0.29 times of those of the β-$NaYF_4$:Yb/Er nanorods, respectively. This big UC luminescence difference can be easily seen from the digital pictures of their according colloidal solutions, as shown in Fig. 3b and d.

To investigate the number of photons involved in the UC process of the samples, the pumping power dependence of the UC luminescence intensity was investigated. UC is a nonlinear process, and it will not maintain its nonlinear behavior up to infinite excitation energies. Hence at high excitation densities, the power dependence of the UC luminescence intensity will become linear, and a "saturation" of the luminescence intensity happens, *i.e.*, linear Er^{3+} UC emissions are observed.[45] For an unsaturated UC process, the emission intensity (I_f) is proportional to the power (n) of the infrared excitation (P) power: $I_f \propto P^n$, where n is the number of infrared photons absorbed per visible photon emitted. In Fig. 4a we can see that the value of n is 1.54, 1.77, 1.59 and 2.17 for the $^4S_{3/2} \rightarrow {}^4I_{15/2}$, $^4F_{9/2} \rightarrow {}^4I_{15/2}$, $^2H_{11/2} \rightarrow {}^4I_{15/2}$, and $^2H_{9/2} \rightarrow {}^4I_{15/2}$ emissions, respectively. This means that the population of the $^4S_{3/2}$, $^4F_{9/2}$, $^2H_{11/2}$, and $^2H_{9/2}$ states came from two-, two-, two- and three- photon UC processes, respectively.[27,45,46] In the case of β-$NaYF_4$:Yb/Er, the crystal lattice parameters are $a = b = 0.596$ nm and $c = 0.353$ nm (JCPDS card 16-0334), and such a structure favors much more the $^4S_{3/2} \rightarrow {}^4I_{15/2}$ and $^2H_{11/2} \rightarrow {}^4I_{15/2}$ transition than those of the $^2H_{9/2} \rightarrow {}^4I_{15/2}$ and $^4F_{9/2} \rightarrow {}^4I_{15/2}$ process, which results in strong green UC emission and explains why the green color is observed in Fig. 3d.

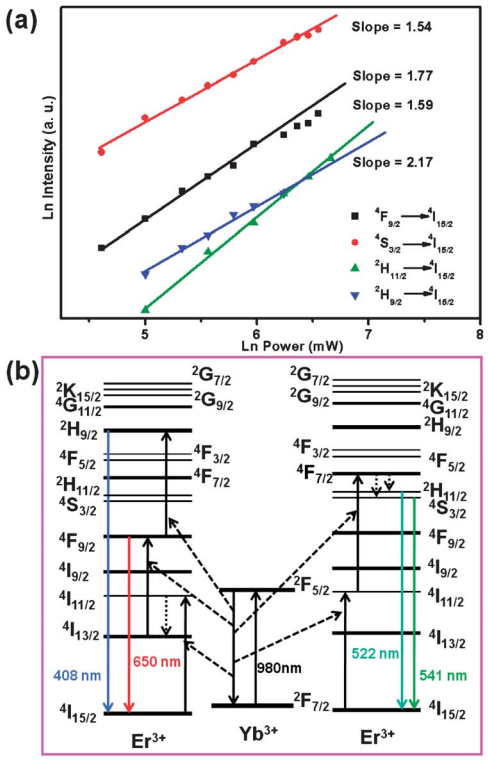

Fig. 4 (a) Power dependence and (b) the UC process of the KSc_2F_7:Yb/Er nanorods.

The energy level diagrams of Er^{3+} and Yb^{3+} ions as well as the UC mechanism are presented in Fig. 4b.[23] The excitation from the 980 nm laser is absorbed by Yb^{3+} ions, the electrons of Er^{3+} ions are first excited from the $^4I_{15/2}$ ground-state to the $^4I_{11/2}$ level ($^4I_{15/2} \rightarrow {}^4I_{11/2}$, Er^{3+}) *via* excitation energy transfer from Yb^{3+} to Er^{3+} ions and then to the $^4F_{7/2}$ level ($^4I_{11/2} \rightarrow {}^4F_{7/2}$, Er^{3+}) by absorbing the energy of another electron from Yb^{3+} ions ($^2F_{5/2}$). The excited electrons of the $^4F_{7/2}$ (Er^{3+}) level then decay to the emitting $^4S_{3/2}$ and $^2H_{11/2}$ levels, mainly through a non-radiative process, and the green $^4S_{3/2} \rightarrow {}^4I_{15/2}$ and $^2H_{11/2} \rightarrow {}^4I_{15/2}$ emissions occur. UC to the $^4F_{9/2}$ state resulting in the $^4F_{9/2} \rightarrow {}^4I_{15/2}$ transition (centered at 650 nm) occurs *via* a two photon process. That is, it occurs *via* two successive energy transfers from Yb^{3+} ions in the $^2F_{5/2}$ excited states. Specifically, an excited Yb^{3+} in the $^2F_{5/2}$ excited state transfers its energy nonresonantly to an Er^{3+} ion in the $^4I_{15/2}$ ground-state thereby exciting it to the $^4I_{11/2}$ excited state, after which it decays nonradiatively to the $^4I_{13/2}$ excited state. A second Yb^{3+} ion in the close vicinity then transfers its energy to the Er^{3+} ion exciting it from the $^4I_{13/2}$ to the $^4F_{9/2}$ excited state, where it can emit a 650 nm photon radiatively following relaxation to the ground state. A third 980 nm photon, or energy transfer from Yb^{3+} to Er^{3+} in the $^4F_{9/2}$ excited state populates the $^2H_{9/2}$ level leading to the purple emission of $^2H_{9/2} \rightarrow {}^4I_{15/2}$.

4 Conclusions

In summary, we have synthesized the highly uniform and well-defined KSc_2F_7:Yb/Er nanorods with intense red UC emission.

Our experimental results indicated that low F^- content and high reaction temperature are favorable for the epitaxial growth of uniform KSc_2F_7:Yb/Er nanorods. This study provides more alternatives of rare earth nanorods with strong red UC emission, and further complements the exploration of Sc-based nanomaterials, which may have unique applications that the Y/Ln-based nanoparticles don't possess.

Acknowledgements

J.J.Z. gratefully appreciate the support from the National Basic Research Program (2011CB933502) of China, and the National Natural Science Foundation (21020102038, 21121091). L.H. thanks the financial support from the Academic Research Fund (Tier 1) from the Singapore Ministry of Education (RG 20/09) and the research grant from the "Jiangsu Specially-Appointed Professors Program", China.

Notes and references

1 Y. Liu, S. Zhou, D. Tu, Z. Chen, M. Huang, H. Zhu, E. Ma and X. Chen, *J. Am. Chem. Soc.*, 2012, **134**, 15083.
2 T. Maldiney, C. Richard, J. Seguin, N. Wattier, M. Bessodes and D. Scherman, *ACS Nano*, 2011, **5**, 854.
3 G. Tian, Z. Gu, L. Zhou, W. Yin, X. Liu, L. Yan, S. Jin, W. Ren, G. Xing, S. Li and Y. Zhao, *Adv. Mater.*, 2012, **24**, 1226.
4 F. Zhang, R. Che, X. Li, C. Yao, J. Yang, D. Shen, P. Hu, W. Li and D. Zhao, *Nano Lett.*, 2012, **12**, 2852.
5 H. Tan, B. Liu and Y. Chen, *ACS Nano*, 2012, **6**, 10505.
6 C. Bouzigues, T. Gacoin and A. Alexandrou, *ACS Nano*, 2011, **5**, 8488.
7 G. Y. Chen, H. L. Qiu, R. W. Fan, S. W. Hao, S. Tan, C. H. Yang and G. Han, *J. Mater. Chem.*, 2012, **22**, 20190.
8 S. Sarkar, B. Meesaragandla, C. Hazra and V. Mahalingam, *Adv. Mater.*, 2013, **25**, 856.
9 F. Wang, X. Xue and X. Liu, *Angew. Chem., Int. Ed.*, 2008, **47**, 906.
10 X. Li, D. Shen, J. Yang, C. Yao, R. Che, F. Zhang and D. Zhao, *Chem. Mater.*, 2012, **25**, 106.
11 S. J. Zeng, J. J. Xiao, Q. B. Yang and J. H. Hao, *J. Mater. Chem.*, 2012, **22**, 9870.
12 G. Gao, C. Zhang, Z. Zhou, X. Zhang, J. Ma, C. Li, W. Jin and D. Cui, *Nanoscale*, 2013, **5**, 351.
13 J. B. Zhao, Z. D. Lu, Y. D. Yin, C. McRae, J. A. Piper, J. M. Dawes, D. Y. Jin and E. M. Goldys, *Nanoscale*, 2013, **5**, 944.
14 L. Cheng, K. Yang, Y. Li, J. Chen, C. Wang, M. Shao, S.-T. Lee and Z. Liu, *Angew. Chem., Int. Ed.*, 2011, **50**, 7385.
15 C. Li and J. Lin, *J. Mater. Chem.*, 2010, **20**, 6831.
16 A. D. Ostrowski, E. M. Chan, D. J. Gargas, E. M. Katz, G. Han, P. J. Schuck, D. J. Milliron and B. E. Cohen, *ACS Nano*, 2012, **6**, 2686.
17 H.-T. Wong, M.-K. Tsang, C.-F. Chan, K.-L. Wong, B. Fei and J. Hao, *Nanoscale*, 2013, **5**, 3465.
18 M. Haase and H. Schäfer, *Angew. Chem., Int. Ed.*, 2011, **50**, 5808.
19 F. Wang and X. Liu, *J. Am. Chem. Soc.*, 2008, **130**, 5642.
20 P. Li, Q. Peng and Y. Li, *Adv. Mater.*, 2009, **21**, 1945.
21 F. Wang, R. Deng, J. Wang, Q. Wang, Y. Han, H. Zhu, X. Chen and X. Liu, *Nat. Mater.*, 2011, **10**, 968.
22 Y. Liu, D. Tu, H. Zhu, R. Li, W. Luo and X. Chen, *Adv. Mater.*, 2010, **22**, 3266.
23 M. He, P. Huang, C. Zhang, H. Hu, C. Bao, G. Gao, R. He and D. Cui, *Adv. Funct. Mater.*, 2011, **21**, 4470.
24 G. Chen, T. Y. Ohulchanskyy, A. Kachynski, H. Ågren and P. N. Prasad, *ACS Nano*, 2011, **5**, 4981.
25 V. Mahalingam, R. Naccache, F. Vetrone and J. A. Capobianco, *Chem. Commun.*, 2011, **47**, 3481.
26 J. Wang, F. Wang, C. Wang, Z. Liu and X. Liu, *Angew. Chem., Int. Ed.*, 2011, **50**, 10369.
27 G. Wang, Q. Peng and Y. Li, *J. Am. Chem. Soc.*, 2009, **131**, 14200.
28 H. Qiu, G. Chen, L. Sun, S. Hao, G. Han and C. Yang, *J. Mater. Chem.*, 2011, **21**, 17202.
29 F. Vetrone, V. Mahalingam and J. A. Capobianco, *Chem. Mater.*, 2009, **21**, 1847.
30 X. Teng, Y. Zhu, W. Wei, S. Wang, J. Huang, R. Naccache, W. Hu, A. I. Y. Tok, Y. Han, Q. Zhang, Q. Fan, W. Huang, J. A. Capobianco and L. Huang, *J. Am. Chem. Soc.*, 2012, **134**, 8340.
31 L. Wang, P. Li and Y. Li, *Adv. Mater.*, 2007, **19**, 3304.
32 F. Wang, Y. Han, C. S. Lim, Y. Lu, J. Wang, J. Xu, H. Chen, C. Zhang, M. Hong and X. Liu, *Nature*, 2010, **463**, 1061.
33 J. Yang, Y. Deng, Q. Wu, J. Zhou, H. Bao, Q. Li, F. Zhang, F. Li, B. Tu and D. Zhao, *Langmuir*, 2010, **26**, 8850.
34 S. Ye, Y.-j. Li, D.-c. Yu, G.-p. Dong and Q.-Y. Zhang, *J. Mater. Chem.*, 2011, **21**, 3735.
35 Y. Huang, H. You, G. Jia, Y. Zheng, Y. Song, M. Yang, K. Liu and L. Zhang, *J. Phys. Chem. C*, 2009, **113**, 16962.
36 J. Yang, C. Zhang, C. Peng, C. Li, L. Wang, R. Chai and J. Lin, *Chem.–Eur. J.*, 2009, **15**, 4649.
37 C. Liu, H. Wang, X. Li and D. Chen, *J. Mater. Chem.*, 2009, **19**, 3546.
38 X. G. Peng, *Adv. Mater.*, 2003, **15**, 459.
39 H.-X. Mai, Y.-W. Zhang, L.-D. Sun and C.-H. Yan, *J. Phys. Chem. C*, 2007, **111**, 13721.
40 J. Zhang, Z. Lin, Y. Lan, G. Ren, D. Chen, F. Huang and M. Hong, *J. Am. Chem. Soc.*, 2006, **128**, 12981.
41 M. Ethayaraja and R. Bandyopadhyaya, *Langmuir*, 2007, **23**, 6418.
42 Z. Lin, B. Gilbert, Q. Liu, G. Ren and F. Huang, *J. Am. Chem. Soc.*, 2006, **128**, 6126.
43 X. Liang, X. Wang, J. Zhuang, Q. Peng and Y. Li, *Adv. Funct. Mater.*, 2007, **17**, 2757.
44 L. Wang and Y. Li, *Chem. Mater.*, 2007, **19**, 727.
45 M. Pollnau, D. R. Gamelin, S. R. Luthi, H. U. Gudel and M. P. Hehlen, *Phys. Rev. B: Condens. Matter*, 2000, **61**, 3337.
46 G. Y. Chen, Y. Liu, Z. G. Zhang, B. Aghahadi, G. Somesfalean, Q. Sun and F. P. Wang, *Chem. Phys. Lett.*, 2007, **448**, 127.

